

Nanoscale

Accepted Manuscript



This is an *Accepted Manuscript*, which has been through the Royal Society of Chemistry peer review process and has been accepted for publication.

Accepted Manuscripts are published online shortly after acceptance, before technical editing, formatting and proof reading. Using this free service, authors can make their results available to the community, in citable form, before we publish the edited article. We will replace this *Accepted Manuscript* with the edited and formatted *Advance Article* as soon as it is available.

You can find more information about *Accepted Manuscripts* in the [Information for Authors](#).

Please note that technical editing may introduce minor changes to the text and/or graphics, which may alter content. The journal's standard [Terms & Conditions](#) and the [Ethical guidelines](#) still apply. In no event shall the Royal Society of Chemistry be held responsible for any errors or omissions in this *Accepted Manuscript* or any consequences arising from the use of any information it contains.

Cite this: DOI: 10.1039/c0xx00000x

www.rsc.org/xxxxxx

ARTICLE TYPE

Hierarchical Ni@Fe₂O₃ Superparticles through Epitaxial Growth of γ -Fe₂O₃ Nanorods on *in situ* Formed Ni Nanoplates

Muhammad Nawaz Tahir,^{a*} Jana Herzberger,^b Filipe Natalio,^{a†} Oskar Köhler,^a Robert Branscheid,^c Enrico Mugnaioli,^c Vadim Ksenofontov,^a Martin Panthöfer,^a Ute Kolb,^c Holger Frey^b and Wolfgang Tremel^{a*}

Received (in XXX, XXX) Xth XXXXXXXXX 20XX, Accepted Xth XXXXXXXXX 20XX

DOI: 10.1039/b000000x

One endeavour of nanochemistry is the bottom-up synthesis of functional mesoscale structures from basic building blocks. We report a one-pot wet chemical synthesis of Ni@ γ -Fe₂O₃ superparticles containing Ni cores densely covered with highly oriented γ -Fe₂O₃ (maghemite) nanorods (NRs) by controlled reduction/decomposition of nickel acetate (Ni(ac)₂) and Fe(CO)₅. Automated diffraction tomography (ADT) of the Ni-Fe₂O₃ interface in combination with Mössbauer spectroscopy showed that selective and oriented growth of the γ -Fe₂O₃ nanorods on the Ni core is facilitated through the formation of a Fe_{0.05}Ni_{0.95} alloy and the appearance of superstructure features that may reduce strain at the Ni-Fe₂O₃ interface. The common orientation of the maghemite nanorods on the Ni core of the superparticles leads to a greatly enhanced magnetization. After functionalization with a catechol-functional polyethylene glycol (C-PEG) ligand the Ni@ γ -Fe₂O₃ superparticles were dispersible in water.

Introduction

Nano-heterostructures containing chemically distinct components have great potential for advancing nanomaterial research by providing a means to define diverse functionalities within single nanoparticles.¹ Moreover, new properties that do not exist in the individual components may arise from strong interfacial interactions at the nanoscale. In recent years, some progress has been made concerning the fabrication of nanocomposites with spherical,² coaxial core-shell,³ or one- and two-dimensional (1D and 2D) heterojunction structures.⁴⁻⁶ To explore potential applications, architecturally assembling of primary nano-building blocks into specific geometric forms is needed. However, despite a few reported hierarchical complex structures⁷⁻¹³ a general scheme for the controlled organization and the preferential crystallographic orientation of the secondary structure is lacking. Therefore it would be desirable to obtain nanostructured materials, where the individual units, each of them characterized by its particular physical properties, surface chemistry and morphology, can be combined into a single nano-object. In the realm of nanostructures there are examples of architectures based on inorganic materials, such as nanowire superlattices,¹⁴ or multilayered nanowires.^{15,16} A central target of colloidal nanocrystal research is to create similar - or even more complex - structures while leveraging the advantages of solution-phase fabrication, such as low-cost synthesis and compatibility in disparate environments. Important fundamental components could be catalyti-

cally active metals like Ni,¹⁷ Pd¹⁸ or Pt¹⁹ and magnetic metal oxides like Fe₂O₃²⁰ or Fe₃O₄.¹⁹

The chemical functionality of the individual components allows studying the assembly of such hetero-nanostructures.²¹ Multi-component core@shell,²² yolk@shell²³ or phase-segregated heterodimer^{24,25} particles or materials containing metal and magnetic metal oxide components with different compositions like Pt@Fe₃O₄,²⁶ Au@Fe₃O₄,²⁷⁻²⁹ FePt@MnO,³⁰ Ag@Fe₃O₄,³¹ Au@MnO₃³² or Au@MnO@SiO₂³³ have attracted particular attention. The synthesis of these hetero-nanoparticles is facilitated when the interfacial energy is reduced by epitaxial growth, i.e., an extremely thin metallic interlayer forming at the interface, because the two components have similar lattice parameters.³⁴⁻³⁷ The synthesis of nanoparticles by thermolysis of organometallic precursors in the presence of surfactants is a unique tool to control the kinetics of phase equilibria and particle aggregation, because phase formation and ordering of the components at the nanoscale are under molecular control. They depend on (i) the decomposition temperatures of the precursors, (ii) the relative activation energies for nucleation, and (iii) interfacial energies which are dictated by interactions of the surfactant and the solvents with the particle surfaces. Despite tremendous efforts to find a general synthetic access to such heterostructures, it still remains a challenge to prepare nanoparticles with complex structures e.g. superparticles having well-controlled sizes, shapes, compositions, and properties. To the best of our knowledge there is no report for the synthesis of superparticles using colloidal protocols. We have demonstrated the relevance of the precursor decomposition temperature by the selective synthesis of nano-

crystals of the ternary compounds CoFe_2O_4 , CuFe_2O_4 and phase segregated $\text{Co@Fe}_2\text{O}_3$ and $\text{Cu@Fe}_3\text{O}_4$ heteroparticles.^{17,20,38} Based on these findings, we report here the controlled synthesis of colloidal hetero-superparticles consisting of nanoplates densely decorated with highly oriented maghemite ($\gamma\text{-Fe}_2\text{O}_3$, defect spinel) nanorods. Typically, particles in the size range of ~ 200 nm are difficult to solubilize (e.g. using low molecular weight C-PEGs). The catechol moiety is an excellent anchor group for high-valent metal oxide surfaces,³⁹⁻⁴¹ and in combination with PEG ensures excellent solubility of the superparticles in aqueous media. The commonly used established procedures to obtain catechol-functional PEGs are based on coupling chemistry, starting from a dopamine derivative and commercially available functional PEGs, e.g. $\text{NH}_2\text{-PEG}$ or NHS-PEG ,⁴²⁻⁴⁴ but the palette of commercial PEGs with specific end-groups and different molecular weights is limited and can be high-priced. Therefore we use a new synthetic procedure for catechol-functional PEGs based on anionic ring opening polymerization of ethylene oxide (EO) starting from a protected catechol-initiator. This synthetic strategy allows precisely tailoring the chain-length of PEG through the initiator to monomer ratio and guarantees well-defined polymers through the living character of the polymerization. Further, additional functional groups could easily be introduced by various terminating agents or by incorporation of functional epoxides.^{45,46} The as-synthesized superparticles could be solubilized after functionalization with a new catechol-polyethylene glycol (C-PEG) polymer ligand.⁴⁷ After functionalization the superparticles formed stable dispersions in a range of solvents including water.

Experimental

Materials. Iron(0) pentacarbonyl ($\text{Fe}(\text{CO})_5$, 99.5%, Acros), nickel(II) acetate tetrahydrate ($\text{Ni}(\text{ac})_2 \cdot 4\text{H}_2\text{O}$, 99%, Fluka), oleic acid (Aldrich), oleylamine (80-90%, Acros), trioctylphosphine ($[\text{CH}_3(\text{CH}_2)_7]_3\text{P}$, 99% Sigma-Aldrich), ethanol (99.8%, Roth), toluene (>99%, Aldrich), hexane (p.A. Fisher), dichloromethane DCM (p.A. Fisher), dimethylformamide (DMF) (extra dry, >99.8%, Acros), diethyl ether (p.A. Fisher) were used as received without further purification.

Polymer synthesis. Ethylene oxide (99.5%) was purchased from Aldrich and hydrochloric acid (37%) from VWR chemicals. Chloroform-*d* was purchased from Deutero GmbH. All other solvents and reagents were ordered from Acros Organics.

Synthesis of $\text{Ni@}\gamma\text{-Fe}_2\text{O}_3$ superparticles. Hierarchically decorated $\text{Ni@}\gamma\text{-Fe}_2\text{O}_3$ superparticles were synthesized by mixing 62.25 mg (0.25 mmol) of nickel acetate $\text{Ni}(\text{ac})_2$, 7 mL of oleylamine, 1 mmol of trioctyl-phosphine, and 2 mmol of oleic acid and stirring them for 20 min under the inert condition before increasing the temperature. The mixture was heated to 120°C for 20 min. Subsequently, 67.55 μL of $\text{Fe}(\text{CO})_5$ were added and the solution was heated 180°C for 30 min and cooled slowly to room temperature. A black product was precipitated from the solution by adding an excess of ethanol. The precipitate was separated by centrifugation (9000 rpm, 10 min, RT). Finally, the product was dissolved in toluene, flushed with argon (Ar) and stored at +4°C.

Synthesis of catechol initiated PEG by anionic ring opening polymerization of ethylene oxide (CA-PEG). The synthesis of catechol-initiated PEG (CA-PEG) was performed as described

recently.⁴⁷ Under argon atmosphere, 2,2-dimethyl-1,3-benzodioxole-5-propanol (catechol-acetonide-OH, CA-OH) (1 eq, 136.9 mg, 0.66 mmol) and cesium hydroxide ($\text{CsOH} \cdot \text{H}_2\text{O}$) (0.8 eq, 87.9 mg, 0.53 mmol) were suspended in 10 mL of benzene and heated to 60°C for 30 min. Subsequently, the partially deprotonated initiator was evacuated at 55 °C for 12 h. About 15 mL of dry THF (stored over sodium) were cryo-transferred into the flask followed by the addition of 5 mL of DMSO by a syringe. The mixture was stirred for 15 min at room temperature to ensure complete dissolution of the cesium alkoxide, followed by cooling the flask to -80 °C. 2 mL of ethylene oxide (67 eq, 44 mmol) were cryo-transferred into the flask via a graduated ampoule. The polymerization proceeded for 12 h (55 °C) and was stopped by addition of 0.5 mL methanol. The polymer was precipitated into ice cold diethyl ether and separated by a centrifuge, yielding CA-PEG in a quantitative yield.

¹H NMR (CDCl_3 , 400 MHz): δ ($\text{CHCl}_3 = 7.26$ ppm) 6.63-6.56 (m, 3 H, H_{arom}), 3.82-3.41 (m, backbone and $\text{CH}_2\text{-O-PEG}$), 2.57 (t, 2 H, $\text{CH}_2_{\text{benzyl}}$), 1.88-1.79 (m, 2 H, CH_2), 1.65 (s, 6 H, CH_3).

Deprotection of the acetonide group (C-PEG). According to ref. [47], 100 mg of CA-PEG were dissolved in 5 mL of aqueous hydrochloric acid (1 mol/L) and stirred for 12 h, letting the cleaved acetone escape. The solvent was removed under reduced pressure (10^{-3} mbar), and the polymer was dissolved in methanol, precipitated into ice cold diethyl ether and separated by a centrifuge. The yield was quantitative.

¹H NMR (methanol-*d*₄, 400 MHz): δ (MeOH = 3.31 ppm, 4.87 ppm) 6.67-6.62 (m, 2 H, HO-C- CH_{arom}), 6.51-6.48 (m, 1 H, CH_{arom}), 3.82-3.41 (m, backbone and $\text{CH}_2\text{-O-PEG}$), 2.53 (t, 2 H, $\text{CH}_2_{\text{benzyl}}$), 1.84-1.78 (m, 2 H, CH_2).

Surface functionalization of $\text{Ni@}\gamma\text{-Fe}_2\text{O}_3$ superparticles with CA-PEG. 20 mg of $\text{Ni@}\gamma\text{-Fe}_2\text{O}_3$ superparticles dispersed in 20 mL of chloroform were dropped slowly over 1 h into the above synthesized polymer solution (40 mg/ 10mL, of chloroform). The reaction was continuously stirred at room temperature for 5 h under inert conditions. The functionalized nanoparticles were precipitated by addition of hexane (90 mL) und separated from unbound polymer and surfactants by centrifugation. The $\text{Ni@}\gamma\text{-Fe}_2\text{O}_3$ superparticles were washed twice by dispersing them in a mixture of chloroform, hexane (1:3) and by phase transferring into water.

Physical Characterization

Electron Microscopy. The size and morphology of the as-synthesized $\text{Ni@}\gamma\text{-Fe}_2\text{O}_3$ NPs were investigated using transmission electron microscopy (TEM, Philips EM 420 with an acceleration voltage of 120 kV). Samples for TEM were prepared by placing a drop of dilute NP solution in hexane on a carbon coated copper grid. Low-resolution TEM images were recorded on a Philips EM420 microscope operating at an acceleration voltage of 120 kV. STEM data and ED patterns were obtained on a FEI Tecnai F30 S-TWIN with a 300 kV field emission gun.

X-Ray Diffraction. XRD measurements were performed on a Bruker D8 Advance diffractometer equipped with a Sol-X energy-dispersive detector and operating with Mo $\text{K}\alpha$ radiation. Crystalline phases were identified according to the PDF-2 database, using Bruker AXS EVA 10.0 software. Full profile fits on the basis of the crystal structural models^{48,49} were performed

with TOPAS Academic 4.1^{50,51} applying the fundamental parameter approach.

Mössbauer Spectroscopy and Magnetic Susceptibility Measurements. Mössbauer spectra were obtained at room temperature, 150 K, 87.5 K and 4.2 K with a constant acceleration transmission Mössbauer spectrometer and a ⁵⁷Co (Rh) source. An α -Fe foil was used to calibrate the Mössbauer spectrometer in a velocity range of ± 10 mms⁻¹. Magnetic measurements were carried out using a Quantum Design MPMS-XL SQUID (superconducting quantum interference device) magnetometer.

Automated electron diffraction tomography (ADT).

Automated electron diffraction tomography (ADT) is a method for *ab initio* structure analysis of nanocrystals. ADT allows fine sampling of the reciprocal space by sequential collection of electron diffraction patterns while tilting a nanocrystal in fixed tilt steps around an arbitrary axis. Electron diffraction is collected in nano diffraction mode (NED) with a semi-parallel beam with a diameter down to 50 nm. For crystal tracking micro-probe STEM imaging is used. Full automation of the acquisition procedure allowed optimization of the electron dose distribution and therefore analysis of highly beam sensitive samples. Cell parameters, space group and reflection intensities can be determined directly within a reconstructed 3d diffraction volume using a dedicated software package (ADT3D). Intensity data sets extracted from such a volume usually show a high coverage and significantly reduced dynamical effects due to “off-zone” acquisition. The use of this data for “*ab initio*” structure solution by direct methods implemented in standard programs for X-ray crystallography is demonstrated. NED, automated diffraction tomography (ADT) and HRTEM were used for crystallographically characterizing the superparticles. Automated electron diffraction tomography (ADT) is a method for *ab initio* structure analysis of nanocrystals,^{52,53} which allows fine sampling of the reciprocal space by sequential collection of electron diffraction patterns while tilting a nanocrystal in fixed tilt steps around an arbitrary axis. Electron diffraction is collected in nano diffraction mode (NED) with a semi-parallel beam with a diameter down to 20-50 nm.⁵⁴

¹H NMR. ¹H NMR spectra (400 MHz) were recorded using a Bruker Avance III HD 400 apparatus operated at 400 MHz with a 5 mm BBFO-SmartProbe (Z-gradient) and an ATM as well as a SampleXpress 60 auto sampler. GPC measurements were performed in DMF (containing 0.25 g·L⁻¹ lithium bromide as an additive). An Agilent 1100 Series was used as an integrated instrument, including a PSS HEMA column (106/105/104 g·mol⁻¹), a UV (275 nm) and a RI detector. Calibration was carried out using poly(ethylene glycol) standards purchased from Polymer Standards Service.

Results and Discussion

Synthesis of Ni@ γ -Fe₂O₃ superparticles. The synthesis of the Ni@ γ -Fe₂O₃ superparticles with a central Ni nanoplate core (~100 nm) and γ -Fe₂O₃ (~30 nm) nanorods domains is illustrated in Fig. 1. In the first step, Ni nanoparticles were nucleated homogeneously via co-reduction by heating nickel acetate, Ni(ac)₂, in the presence of iron pentacarbonyl, Fe(CO)₅, at 120°C. The emerging Ni nuclei transformed to Ni nanoplates (confirmed by examining aliquots at 140°C) still significantly below the de-

composition temperature (T = 180°C) of Fe(CO)₅. In the final heating step at 180°C γ -Fe₂O₃ nanorods grew epitaxially on the preformed Ni nanoplates. The products were precipitated and separated by centrifugation (9000 rpm, 10 min, RT).

Polymer synthesis. The as-synthesized superparticles were functionalized using catechol-polyethylene glycol (C-PEG) polymer ligands⁴⁷ (Scheme S1), which were characterized by ¹H NMR spectroscopy and GPC (Fig. S1-2). The C-PEG ligands were synthesized via anionic ring opening polymerization of ethylene oxide (EO) starting from a protected catechol-initiator. This synthetic strategy allows a precise tailoring of the chain-length of PEG through the initiator to monomer ratio and guarantees well-defined polymers because of the living character of the polymerization.⁴⁷ A cartoon of a C-PEG functionalized Ni@Fe₂O₃ superparticle is shown in Fig. 1. It is worth mentioning that particles of this size (~200 nm) cannot be solubilized using low molecular weight C-PEGs. After functionalization the superparticles were easily dispersible in water; the dispersions were stable for several weeks.

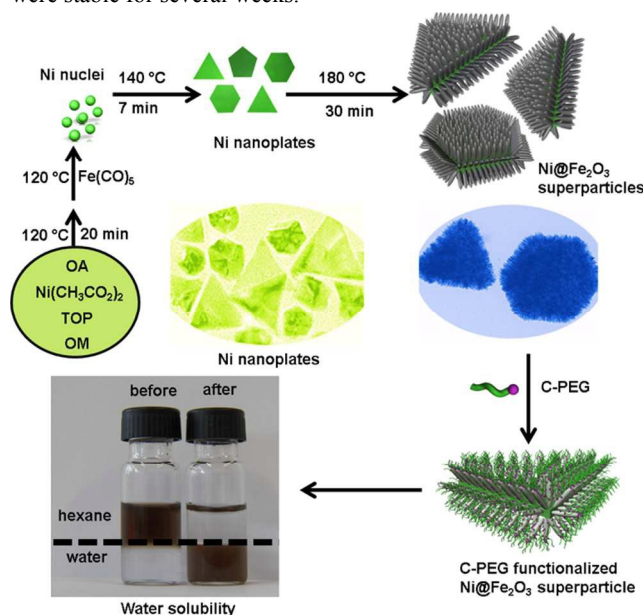


Fig. 1. Synthesis of Ni@ γ -Fe₂O₃ superparticles. Initial Ni nuclei obtained by thermolysis of Ni(ac)₂ transform to Ni nanoplates with a Ni_{1-x}Fe_x interlayer in the presence of Fe(CO)₅, from which highly oriented γ -Fe₂O₃ rods grow epitaxially (OM stands for oleylamine, TOP for trioctyl-phosphine, and OA for oleic acid). The resulting Ni@ γ -Fe₂O₃ superparticles are functionalized with a catechol-polyethylene glycol (C-PEG) ligand to achieve water solubility.

Superparticle growth mechanism. The growth of the Ni@ γ -Fe₂O₃ superparticles was monitored by taking “snapshots” at given time intervals using transmission electron microscopy (TEM). After ~6 minutes plate-like structures were formed (Fig. 2a,b). High-resolution transmission electron microscopy (HRTEM) images revealed that the smallest particles (20-30 nm) were polycrystalline, often displaying penta-twinned structures (Fig. 2a), whereas larger plate-like particles (30-80 nm) had a well-defined triangular morphology. EDX showed the particles to have a composition Fe_{0.05}Ni_{0.95} (Fig. S3). They were single crystalline (shown by HRTEM and nano-electron diffraction (NED)) with a hexagonal pattern and *d*-values of 2.2(1) Å (Fig.

2b,c). At this stage, all particles had a flat triangular or hexagonal habit in agreement with an earlier report by Leng et al.⁵⁵ and a composition of $\text{Fe}_{0.05}\text{Ni}_{0.95}$ as determined by NED, ADT and energy-dispersive X-ray spectroscopic EDX.

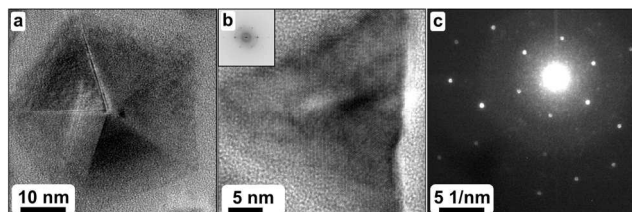


Fig. 2. Growth mechanism: $\text{Fe}_{0.05}\text{Ni}_{0.95}$ precursors after a reaction time of 5 minutes. (a) HRTEM of a pentagonally twinned particle. (b) HRTEM image and (c) NED of a single-crystal flat particle displaying a hexagonal pattern with d -distances of $2.2(1) \text{ \AA}$.

10 When heating slowly to 180°C , $\gamma\text{-Fe}_2\text{O}_3$ nanorods started nucleating on the $\text{Fe}_{0.05}\text{Ni}_{0.95}$ cores. Their growth proceeded anisotropically (Fig. 3a). To show a better overview, an SEM image is provided Fig. S4. The image further confirms hierarchical arrangements of nanodomains in three dimensional (3D) patterns.
15 EDX line profiles taken across the superparticles showed the rods to consist of Fe_2O_3 nanorods decorating a core of metallic Ni plates containing a minor amount of Fe (Fig. 3b). The corresponding STEM image (Fig. 3c) confirms the presence of $\text{Fe}_{0.05}\text{Ni}_{0.95}$ cores and hierarchically grown Fe_2O_3 nanorods.
20 Initially the rods covered only the flat surfaces of the $\text{Fe}_{0.05}\text{Ni}_{0.95}$ cores and grew perpendicular to the cores (Fig. 3d).

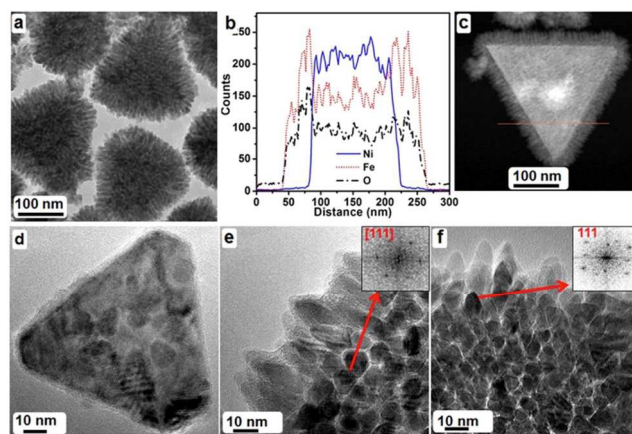


Fig. 3. Growth of $\text{Ni}@ \gamma\text{-Fe}_2\text{O}_3$ superparticles. (a) Zoom of a superparticle showing preferential orientation of the rods growing on the large flat surfaces and the scattered orientation of the rods growing on the core side. (b) An EDX scan (along the red line) confirmed the elemental composition of the superparticle with the aid of a z -contrast image (STEM). (c) Corresponding $\text{Ni}@ \gamma\text{-Fe}_2\text{O}_3$ superparticle. (d) HRTEM of a superparticle at an early stage with nucleated domains of $[111]$ oriented Fe_2O_3 . (e) HRTEM image of a superparticle showing rods growing on the main surface of the Ni plate and viewed along the main direction of growth, i.e. $[111]$. (f) HRTEM image showing rods growing on the side of the Ni plate with vector 111 pointing along out from the superparticle.

35 In Fig. S5 a z -contrast image from an upright standing plate gives a side view of the superparticles. The strong contrast difference between the Fe_2O_3 decoration and the very bright Ni plates was confirmed by energy-dispersive X-ray spectroscopic

(EDX) line scan analysis. The average plate thickness was about
40 10 nm; this could be shown for many plates of different lateral size by tilting the sample. As the supercrystals kept growing, additional rods appeared on the side of the $\text{Fe}_{0.05}\text{Ni}_{0.95}$ cores with a less ordered orientation. The fully-grown nanorods were about 10 nm in diameter and about 30 nm in length (Fig. 3e). HRTEM
45 images confirmed the main direction of the rod growth to be always $[111]$. Most nanorods developed orthogonally to the surface of the Ni plate, showing in projection a typical hexagonal base (Fig. 3e). Other rods grow on the lateral side of the Ni plate, with the $[111]$ vector pointing out from the superparticle surface.
50 The size and density of the $\gamma\text{-Fe}_2\text{O}_3$ nanorods could be controlled by varying the concentration of the $\text{Fe}(\text{CO})_5$ precursor in solution. The TEM images in Fig. 4a,b show that by reducing the concentration of $\text{Fe}(\text{CO})_5$ the size and density of the $\gamma\text{-Fe}_2\text{O}_3$ nanorods decreased (Fig. 4a), whereas an increase of the
55 $\text{Fe}(\text{CO})_5$ concentration induced the formation of dense and almost 100 nm long $\gamma\text{-Fe}_2\text{O}_3$ nanorods (Fig. 4b). However, when $\text{Fe}(\text{CO})_5$ was injected at 180°C , i.e. the decomposition temperature of $\text{Fe}(\text{CO})_5$, a mixture of Ni plates and iron oxide nanoparticles (Fig. S6a) was obtained. Further increasing the injection
60 temperature to 240°C lead to the formation of core-shell nanoparticles, because the Ni cores had adopted already a spherical shape (Fig. S6b). When the amount of $\text{Fe}(\text{CO})_5$ was reduced to $10 \mu\text{l}$, the reduction of the nickel precursor was incomplete, and agglomerated iron oxide nanostructures were formed (Fig. S6c),
65 whereas the injection of excess $\text{Fe}(\text{CO})_5$ lead to the formation of $\text{Ni}@ \gamma\text{-Fe}_2\text{O}_3$ superparticles with iron oxide nanorods ~ 100 nm long and also isolated iron oxide nanoparticles (Fig. S6d). The reaction in the absence of $\text{Fe}(\text{CO})_5$ did not allow a reduction of Ni as indicated by the color of solution even after heating to
70 180°C for 30 min (Fig. S7).

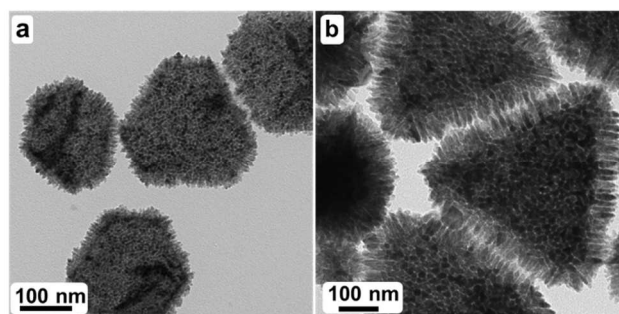


Fig. 4. (a, b) In order to control the density and size of the $\gamma\text{-Fe}_2\text{O}_3$ domains the concentration of the $\text{Fe}(\text{CO})_5$ was reduced (a) and increased (b).

75 The superparticle formation is therefore clearly a hierarchical assembly, as the oxidation of Fe starts only after the Ni-based cores are fully developed. Selected area electron diffraction (SAED) patterns taken either from triangular or hexagonal superparticles could be fully described using two different lattices
80 (Fig. 5a,b). One lattice is consistent with that already observed for the plate-like precursor, i.e. two d distances of $2.2(1) \text{ \AA}$ crossing at 60° . The second lattice is also hexagonal, with d values of $3.0(1) \text{ \AA}$, and it is iso-oriented with respect to the first one.

$\text{Ni}@ \gamma\text{-Fe}_2\text{O}_3$ superparticle structure. ADT^{52,53} was used to
85 obtain a three-dimensional diffraction reconstruction from four independent superparticles (Fig. 5c,d). The reconstructions were

equivalent for triangular and hexagonal shapes. Besides diffuse scattering, presumably produced by randomly oriented γ -Fe₂O₃ rods, two single crystal lattices could be identified (Fig. 5). The first lattice (LAT1) corresponds to a face-centered cubic cell with $a = 8.4(1)$ Å, consistent with the maghemite (γ -Fe₂O₃) cell. The second lattice (LAT2) corresponds to a primitive hexagonal cell with $a = 2.55(5)$ Å and $c = 6.2(1)$ Å. The orientation of the two lattices is correlated, as (111)* and (-211)* reciprocal vectors of LAT1 are respectively parallel to the (001)* and (100)* vectors of LAT2. Vectors LAT1(111)* and LAT2(001)* are perpendicular to the plane of the Ni core, while vectors LAT1(-211)* and LAT2(100)* point to the vertexes of the triangles and vectors LAT1(-110)* and LAT2(110)* point to the vertexes of the hexagons (Fig. S8).

The cubic lattice LAT1 is associated with the γ -Fe₂O₃ nanorods growing perpendicular to the surface of the Fe_{0.05}Ni_{0.95} cores. They produce a single crystal-type pattern, because they have the same orientation. HRTEM images confirm the main direction of the rod growth to be always [111] (Fig. 3f). The hexagonal pattern LAT2 is associated with the triangular (or hexagonal) Fe_{0.05}Ni_{0.95} cores. This lattice is commensurate with the face-centered cubic lattice of metallic Ni, with $a \sim 3.6$ Å, but the cubic symmetry is reduced by additional reflections at $(\frac{1}{3}, \frac{1}{3}, \frac{1}{3})$ and $(\frac{2}{3}, \frac{2}{3}, \frac{2}{3})$ (Fig. S9). These additional reflections may be rationalized by a superstructure induced by the insertion of Fe in the Ni structure, or by a 2-fold rotational twinning of the Ni structure along [111]. The precision of ADT precision does not allow resolving the small deviations between the cell dimensions of Ni and Fe_{0.05}Ni_{0.95}.

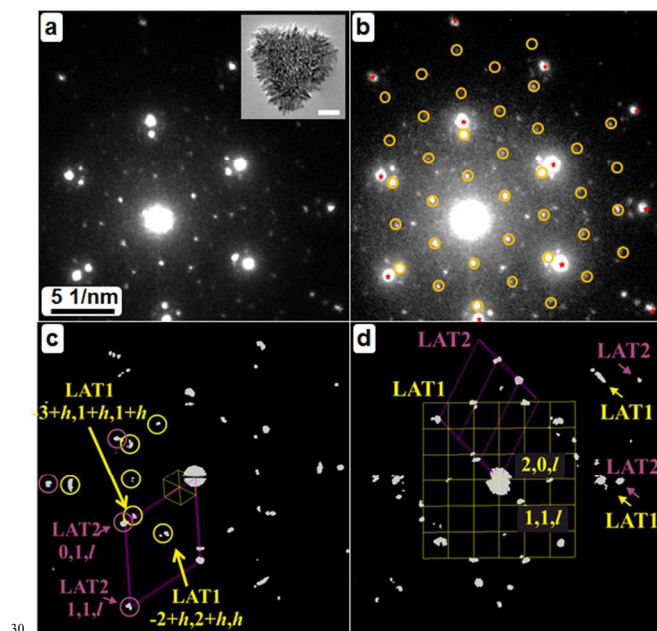


Fig. 5. NED and ADT characterization of mature Fe_{0.05}Ni_{0.95}@ γ -Fe₂O₃ superparticles. (a) NED pattern from the particle inset (scale bar = 50 nm). (b) The pattern could be indexed with two hexagonal patterns with d values of 3.0(1) Å (in yellow) and 2.2(1) Å (in violet), respectively. (c) ADT 3D diffraction reconstruction viewed along the vertical and (d) along a lateral side. The two lattices identified by ADT are sketched in yellow (LAT1) and violet (LAT2).

The presence of maghemite (γ -Fe₂O₃, defect spinel) in the samples was confirmed by powder x-ray diffraction (P-XRD). The

XRD patterns of the Ni@ γ -Fe₂O₃ superparticles displayed broad Bragg maxima indicative of small crystallite sizes (Fig. 6a). Due to reflection broadening, reflection overlap between the Ni and the γ -Fe₂O₃ phase and the high similarity of the corresponding line-patterns a quantitative phase analysis was performed by full pattern profile analysis (“Rietveld refinement”) to distinguish between all possible phases (γ -Fe₂O₃, magnetite (Fe₃O₄) and nickel ferrite (NiFe₂O₄)).^{56,57} For the Ni nanoplate domains of the Ni@Fe₂O₃ superparticles the crystallite sizes of 8(1) nm from the Rietveld refinement are marginally larger for Ni and considerably larger for γ -Fe₂O₃ (21(1) nm). The extra reflections not captured by the Rietveld refinement are due to silicon used as substrate. The Mössbauer spectrum of the Ni@Fe₂O₃ superparticles at 295 K (Fig. 6b) shows a superposition of two magnetic sextets with approximately equal intensities. The component with an isomer shift IS = 0.3(1) mms⁻¹ corresponds to maghemite with an average hyperfine magnetic field of 478 kOe.⁵⁸ A broad magnetic subspectrum with an average hyperfine magnetic field of 433 kOe and IS = 0.6(1) mms⁻¹ can be attributed to the interface region between the pure maghemite phase and the Ni substrate.

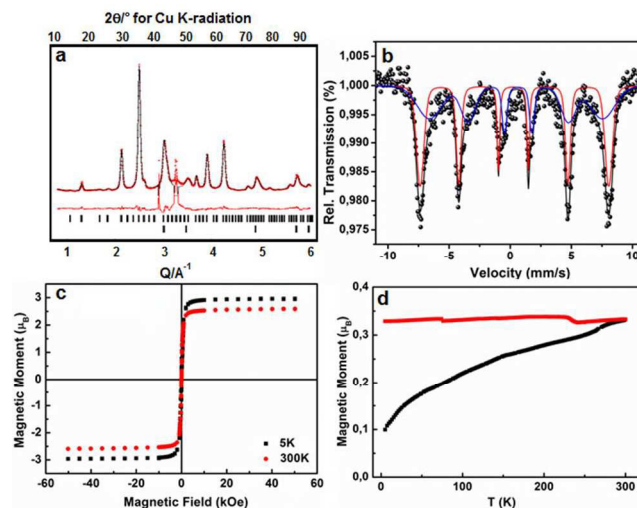


Fig. 6. Particle Characterization. (a) Quantitative phase analysis from the x-ray diffraction pattern of the Ni@ γ -Fe₂O₃ superparticles (red dots: observed intensity, black line: calculated intensity, red line: difference curve; ticks mark the reflection positions of γ -Fe₂O₃ (upper) and elemental Ni (lower)), (b) ⁵⁷Fe Mössbauer spectra of Ni@ γ -Fe₂O₃ superparticles at 295 K. (c, d) Magnetic hysteresis loops at 5 K and 300 K and temperature dependence of the magnetization in field-cooling (FC) and zero-field-cooling (ZFC) of Ni@ γ -Fe₂O₃ superparticle heterodimers.

The magnetic properties of the Ni@ γ -Fe₂O₃ superparticles extracted from the temperature-dependent magnetization and hysteresis curves are shown in Fig. 6c and d. The superparticles are ferrimagnetic at 5 K and superparamagnetic above room temperature. The magnetization curve in Fig. 6c exhibits saturation magnetization values of 2.96 μ_B at 5 K, a value prevailing the expected one of 2.40 μ_B for γ -Fe₂O₃ on a Ni substrate following from the estimation: $2/3 \times 3.33 \mu_B + 1/3 \times 0.62 \mu_B$, where 3.33 μ_B and 0.62 μ_B are saturation magnetizations for γ -Fe₂O₃⁵⁹ and metallic Ni.⁶⁰ This value is also much higher as compared to Ni@ γ -Fe₂O₃ with heterodimer morphology (2.45 μ_B at T = 5 K)¹⁷ and core shell (1.53 μ_B at T = 5 K) as shown in Fig.

S10. The ZFC magnetization increases monotonically with temperature and the FC magnetization shows no significant change. The splitting of the ZFC and FC curves reaches a crossing point around 302 K (Fig. 6d), indicating a blocking temperature above room temperature. The common orientation of the maghemite nanorods on the Ni core of the superparticles leads to a greatly enhanced magnetization because the anisotropy of the superparticles decreases the surface spin canting and disorder, thereby leading to enhanced magnetization. We do not consider interparticle interactions to play a significant role, because the superparticles do not show aggregation (Fig. 3).

3. Conclusion

This work provides a general approach to a new type of magnetic nanocomposite with complex but well-defined mesoscopic architectures through “beaker epitaxy” of basic nano-objects, e.g. for probing the exchange coupling between magnetic particle components at the nanoscale. ADT analysis in combination with Mössbauer spectroscopy indicates that tailoring the interface between the metal and metal oxide components by “alloying” is a key step to the formation of this new kind of colloidal superparticles with multiple well-defined supercrystalline domains under kinetic control. Atom diffusion is eliminated here as rate-limiting step, and only reaction parameters such as interface or precursor structure control the nucleation event.⁶¹ The formation of phase separated Ni@ γ -Fe₂O₃ superparticles is highly unexpected, because Ni is not a noble metal and several stable ternary nickel oxides (e.g. nickel ferrite, NiFe₂O₄) are known, i.e. the nucleation temperature of these ternary phases is not reached under our experimental conditions.

The development of a controlled synthesis of nanocrystalline superparticles is relevant for several reasons: (i) The synthetic approach may be generalized for making nanocrystalline colloidal superparticles with other chemical compositions from organometallic precursors. (ii) The selective growth of the metal oxide nanorods is facilitated through the formation of Ni_{1-x}Fe_x alloy and Fe_{3-x}Ni_xO₄ “buffer layers” (as shown by Mössbauer spectroscopy) at the interface between the Ni core and the γ -Fe₂O₃ rods within the Ni@ γ -Fe₂O₃ superparticles that may serve to reduce strain in a regularly spaced arrangement on the Ni substrate as demonstrated by ADT. The miscibility of most *d* metals with each other in their elemental and oxide structures allows the fabrication of the buffer layer to be generalized. (iii) The properties of the nanocrystalline colloidal superparticles may be modified by “alloying” with other metals or by functionalization with organic molecules. Superparticles may be promising candidates for catalytic¹⁷⁻¹⁹ or electrochemical⁶² applications. Our functionalization strategy uses a well-defined catechol-functional PEG ligand with a tailored chain length and controlled molecular weight obtained from the living polymerization of EO. We anticipate that our findings open many opportunities for assembling particles with complex, but well-defined mesoscopic architectures⁶³ and different magnetic, optical, or chemical properties. This could lead to new multifunctional materials or materials with enhanced performance for a wide range of potential (e.g. sensoric, catalytic) applications.^{64,65}

Acknowledgements

This work was supported in part from the SFB 1066 *Nanodimensionale polymere Therapeutika für die Tumorthherapie*. We thank Dr. Teuta Gasi for support with the Mössbauer spectroscopy.

Notes and references

- ^a Institut für Anorganische Chemie und Analytische Chemie der Johannes Gutenberg-Universität, Duesbergweg 10-14, D-55099 Mainz, Germany
[†] present address:
⁶⁵ Institut für Chemie - Anorganische Chemie, Martin-Luther-Universität Halle-Wittenberg, Kurt-Mothes-Str. 2, 06120 Halle (Germany)
^b Institut für Organische Chemie, Johannes-Gutenberg-Universität Duesbergweg 10-14, D-55099 Mainz, Germany.
^c Institut für Physikalische Chemie, Johannes-Gutenberg-Universität Welderweg 15, D-55099 Mainz, Germany.
- Corresponding Authors: tahir@uni-mainz.de; tremel@uni-mainz.de
[†] Electronic Supplementary Information (ESI) available: Synthesis scheme of catechol-PEG (Scheme S1), GPC trace (RI, DMF, PEG standard) of CA-PEG₆₇ (Figure S1) ¹H NMR spectrum (400 MHz, methanol-*d*₄) of catechol-PEG (C-PEG₆₇) (Figure S2), EDX spectrum of Ni_{0.95}Fe_{0.05} precursors (Figure S3), HRTEM of a superparticle in two view directions (Figure S4), TEM images of Ni_{0.95}Fe_{0.05}@ γ -Fe₂O₃ nanoparticles at different growth stages (Figure S5), digital photograph of reaction mixture at different temperatures (Figure S6), orientation of the lattice of the Ni_{0.95}Fe_{0.05} core with respect to that of triangular and hexagonal superparticles (Figure S7), geometrical relations between hexagonal lattice of the Ni_{0.95}Fe_{0.05} core and cubic cell of Ni (Figure S8), magnetic properties of the Ni@ γ -Fe₂O₃ core shell nanoparticles (Figure S9). See DOI: 10.1039/b000000x/
- H. C. Zeng, *Acc. Chem. Res.* 2013, **46**, 226-235.
 - O. Chen, L. Riedemann, F. Etoc, H. Herrmann, M. Coppey, M. Barch, C. T. Farrar, J. Zhao, O. T. Bruns, H. Wei, P. Guo, J. Cui, R. Jensen, Y. Chen, D. K. Harris, J. M. Cordero, Z. Wang, A. Jasanoff, D. Fukumura, R. Reimer, M. Dahann, R. K. Jain, M. G. Bawendi, *Nat. Commun.* 2014, **5**, 5093.
 - R. G. Chaudhuri, S. Paria, *Chem. Rev.* 2012, **112**, 2373-2433.
 - M. Lattuada, T. A. Hutton, *Nano Today* 2011, **6**, 286-308.
 - M. N. Tahir, F. Natalio, M. A. Cambaz, M. Panthöfer, R. Branscheid, U. Kolb, W. Tremel, *Nanoscale* 2013, **5**, 9944-9949.
 - C. Huang, S. Wu, A. M. Sanchez, J. J. P. Peters, R. Beanland, J. S. Ross, P. Rivera, W. Yao, D. C. Cobden, X. Xu, *Nat. Mater.* 2014, **13**, 1096-1101.
 - J. Y. Lao, J. G. Wen, Z. F. Ren, *Nano Lett.* 2002, **2**, 1287-1291.
 - S. Park, S.-D. Seo, S. Lee, S. W. Seo, K.-S. Park, C. W. Lee, D.-W. Kim, K. S. Hong, *J. Phys. Chem. C* 2012, **116**, 21717-21726.
 - D. F. Zhang, L. D. Sun, C. J. Jia, Z. G. Yan, L. P. You, C. H. Yan, *J. Am. Chem. Soc.* 2005, **127**, 13492-13493.
 - Y. Chen, C. Zhu, X. Shi, M. Cao, H. Jin, *Nanotechnol.* 2008, **19**, 205603.
 - W. Zhou, C. Cheng, J. Liu, Y. Y. Tay, J. Jiang, X. Jia, J. Zhang, H. Gong, H. H. Hong, T. Yu, *Adv. Funct. Mater.* 2011, **21**, 2439-2445.
 - U. K. Gautam, X. Fang, Y. Bando, J. Zhan, D. Golberg, *ACS Nano* 2008, **2**, 1015-1021.
 - M. Shang, W. Wang, W. Yin, J. Ren, S. Sun, L. Zhang, *Chem. Eur. J.* 2010, **16**, 11412-11419.
 - H. J. Fan, P. Werner, M. Zacharias, *Small* 2006, **2**, 700-717.
 - B. R. Martin, D. J. Dermody, B. D. Reiss, M. Fang, L. A. Lyon, M. J. Natan, T. E. Mallouk, *Adv. Mater.* 1999, **11**, 1021-1025.
 - R. D. Robinson, B. Sadtler, D. O. Demchenko, C. K. Erdonmez, L. W. Wang, A. P. Alivisatos, *Science* 2007, **317**, 355-358.
 - B. Nakhjavan, M. N. Tahir, F. Natalio, M. Panthöfer, H. Gao, M. Dietzsch, R. Andre, T. Gasi, V. Ksenofontov, R. Branscheid, U. Kolb, W. Tremel, *Nanoscale* 2012, **4**, 4571-4577.
 - J. Jang, J. Chung, S. Kim, S. W. Jun, B. H. Kim, D. W. Lee, B. M. Kim, T. Hyeon, *Phys. Chem. Chem. Phys.* 2011, **13**, 2512-2516.

- 19 C. Wang, H. Daimon, S. Sun, *Nano Lett.* 2009, **9**, 1493-1496.
- 20 B. Nakhjavan, M. N. Tahir, M. Panthöfer, H. Gao, T. Gasi, V. Ksenofontov, R. Branscheid, S. Weber, U. Kolb, L. M. Schreiber, W. Tremel, *Chem. Commun.* 2011, **47**, 8898-8900.
- 5 21 H. Yu, M. Chen, P. M. Rice, S. X. Wang, R. L. White, S. Sun, *Nano Lett.* 2005, **5**, 379-382.
- 22 J. Kim, J. E. Lee, J. Lee, J. H. Yu, B. C. Kim, K. An, Y. Hwang, C. H. Shin, J. G. Park, T. Hyeon, *J. Am. Chem. Soc.* 2006, **128**, 688-689.
- 10 23 I. Lee, J. B. Joo, Y. Yin, F. Zaera, *Angew. Chem. Int. Ed.* 2011, **50**, 10208-10211.
- 24 M. Casavola, R. Buonsanti, G. Caputo, P. D. Cozzoli, *Eur. J. Inorg. Chem.* 2008, 837-854.
- 25 I. Schick, S. Lorenz, D. Gehrig, K. Fischer, S. Tenzer, H.-J. Schild, D. Strand, F. Laquai, W. Tremel, *Beilstein J. Nanotechnol.* 2014, **5**, 2346-2362.
- 15 26 C. Wang, H. Daimon, S. Sun, *Nano Lett.* 2009, **9**, 1493-1496.
- 27 Y. Wei, R. Klajn, A. O. Pinchuk, B. A. Grzybowski, *Small* 2008, **4**, 1635-1639.
- 20 28 C. Xu, J. Xie, D. Ho, C. Wang, N. Kohler, E. G. Walsh, J. R. Morgan, Y. E. Chin, S. Sun, *Angew. Chem. Int. Ed.* 2008, **47**, 173-176.
- 29 I. Schick, S. Lorenz, D. Gehrig, A.-M. Schilmann, H. Bauer, M. Panthöfer, K. Fischer, M. Schmidt, D. Strand, F. Laquai, W. Tremel, *J. Am. Chem. Soc.* 2014, **136**, 2473-2483.
- 25 30 T. D. Schladt, T. Graf, O. Köhler, H. Bauer, K. Schneider, C. Herold, J. Mertins, W. Tremel, *Chem. Mater.* 2012, **24**, 525-535.
- 31 G. Lopes, J. M. Vargas, S. K. Sharma, F. Beron, K. R. Pirota, M. Knobel, C. Rettori, R. D. Zysler, *J. Phys. Chem. C* 2010, **114**, 10148-10152.
- 30 32 T. D. Schladt, M. I. Shukoor, M. N. Tahir, F. Natalio, K. Schneider, I. Ament, J. Becker, F. Jochum, S. Weber, P. Theato, L. M. Schreiber, C. Sönnichsen, H. C. Schröder, W. E. G. Müller, W. Tremel, *Angew. Chem. Int. Ed.* 2010, **49**, 3976-3980.
- 35 33 I. Schick, D. Gehrig, M. Montigny, B. Balke, M. Panthöfer, A. Henkel, F. Laquai, W. Tremel, *Chem. Mater.* 2015, DOI: 10.1021/acs.chemmater.5b01968.
- 34 C. Wang, C. Xu, H. Zeng, S. Sun, *Adv. Mater.* 2009, **21**, 3045-3052.
- 40 35 L. Carbone, P. D. Cozzoli, *Nano Today* 2010, **5**, 449-493.
- 36 C. Wang, W. Tian, Y. Ding, Y.-Q. Ma, Z. L. Wang, N. M. Markovic, V. R. Stamenkovic, H. Daimon, S. Sun, *J. Am. Chem. Soc.* 2010, **132**, 6524-6529.
- 37 M. R. Buck, J. F. Bondi, R. E. Schaak, *Nat. Chem.* 2011, **4**, 37-44.
- 45 38 B. Nakhjavan, M. N. Tahir, H. Gao, T. Schladt, K. Schneider, F. Natalio, I. Ament, R. Branscheid, S. Weber, H.-C. Schröder, W. E. G. Müller, U. Kolb, C. Sönnichsen, L. M. Schreiber, W. Tremel, *J. Mater. Chem.* 2011, **21**, 8605-8611.
- 39 C. Xu, K. Xu, G. Gu, R. Zheng, H. Liu, X. Zhang, Z. Guo, B. Xu, *J. Am. Chem. Soc.* 2004, **126**, 9938-9939.
- 50 40 M. N. Tahir, M. Eberhardt, P. Theato, S. Faiß, A. Janshoff, T. Gorelik, U. Kolb, W. Tremel, *Angew. Chem. Int. Ed.* 2006, **45**, 908-912.
- 41 J. Sedo, J. Saiz-Poseu, F. Busque, D. Ruiz-Molina, *Adv. Mater.* 2013, **25**, 653-701.
- 55 42 E. Amstad, T. Gillich, I. Bilecka, M. Textor, E. Reimhult, *Nano Lett.* 2009, **9**, 4042-4048.
- 43 B. P. Lee, J. L. Dalsin, P. B. Messersmith, *Biomacromolecules* 2002, **3**, 1038-1047.
- 60 44 J. Su, F. Chen, V. L. Cryns, P. B. Messersmith, *J. Am. Chem. Soc.* 2011, **133**, 11850-11853.
- 45 M. S. Thompson, T. P. Vadala, M. L. Vadala, Y. Lin, J. S. Riffle, *Polymer* 2008, **49**, 345-373.
- 46 B. Obermeier, F. Wurm, C. Mangold, H. Frey, *Angew. Chem. Int. Ed.* 2011, **50**, 7988-7997.
- 65 47 V. S. Wilms, H. Bauer, C. Tonhauser, A. M. Schilmann, M. C. Müller, W. Tremel, H. Frey, *Biomacromolecules* 2013, **14**, 193-199.
- 48 Y. Leng, Y. Li, X. Li, S. Takahashi, *J. Phys. Chem. C* 2007, **111**, 6630-6633.
- 70 49 U. Kolb, T. Gorelik, C. Kübel, M. T. Otten, D. Hubert, *Ultramicroscopy* 2007, **107**, 507-513.
- 50 U. Kolb, T. Gorelik, M. T. Otten, *Ultramicroscopy* 2008, **108**, 763-772.
- 75 51 W. Kelm, W. Mader, *Z. Naturforsch.* 2006, **61b**, 665-671.
- 52 C. Cavalius, K. Moh, S. Mathur, *Cryst. Growth Des.* 2012, **12**, 5948-5955.
- 53 N. N. Greenwood, T. G. Gibb, T. G. Mössbauer *Spectroscopy*; Chapman and Hall Ltd: London, 1971.
- 80 54 H. Lueken, *Magnetochemie, Teubner Studienbücher*, 2000.
- 55 H. Danan, A. Herr, A. J. P. Meyer, *J. Appl. Phys.* 1968, **39**, 669-670.
- 56 D. C. Johnson, *Curr. Opin. Solid State Mater. Sci.* 1998, **3**, 159-167.
- 85 57 B. Oschmann, M. N. Tahir, F. Mueller, D. Bresser, I. Lieberwirth, W. Tremel, S. Passerini, R. Zentel, *Macromol. Rapid Commun.* 2015, **36**, 1075-1082.
- 58 C. Feldmann, *Angew. Chem. Int. Ed.* 2013, **52**, 7610-7611.
- 59 C. Burda, X. Chen, M. A. El-Sayed, *Chem. Rev.* 2005, **105**, 1025-1102.
- 90 60 H. Goesmann, C. Feldmann, *Angew. Chem. Int. Ed.* 2010, **49**, 1362-1395.
- 61 A. Taylor, *J. Inst. Metals* 1950, **77**, 585.
- 62 C. A. Greaves, *J. Solid State Chem.* 1983, **49**, 325-333.
- 95 63 A. Coelho, *TOPAS Academic V 4.1*; Coelho Software: Brisbane, AUS, 2007.
- 64 R. W. Cheary, A. A. Coelho, *J. Appl. Crystallogr.* 1992, **25**, 109-121.
- 65 E. Mugnaioli, I. Andrusenko, T. Schüler, N. Loges, R. E. Dinnebier, M. Panthöfer, W. Tremel, U. Kolb, *Angew. Chem. Int. Ed.* 2012, **51**, 7041-7045.
- 100